CHEMISTRY
A EUROPEAN JOURNAL

DOI: 10.1002/chem.201000660

Material Properties and Structural Characterization of $M_3Si_6O_{12}N_2:Eu^{2+}$ (M = Ba, Sr)—A Comprehensive Study on a Promising Green Phosphor for pc-LEDs

Cordula Braun,[a] Markus Seibald,[a] Saskia L. Börger,[a] Oliver Oeckler,[a] Teak D. Boyko,[b] Alexander Moewes,[b] Gerhard Miehe,[c] Andreas Tücks,[d] and Wolfgang Schnick*[a]

Abstract: The efficient green phosphor $Ba_3Si_6O_{12}N_2:Eu^{2+}$ and its solid-solution series $Ba_{3-x}Sr_xSi_6O_{12}N_2$ (with $x \approx 0.4$ and 1) were synthesized in a radio-frequency furnace under nitrogen atmosphere at temperatures up to 1425 °C. The crystal structure ($Ba_3Si_6O_{12}N_2$, space group $P\bar{3}$ (no. 147), $a = 7.5218(1)$, $c = 6.4684(1)$ Å, $wR2 = 0.048$, $Z = 1$) has been solved and refined on the basis of both single-crystal and powder X-ray diffraction data. $Ba_3Si_6O_{12}N_2:Eu^{2+}$ is a layer-like oxonitridosilicate and consists of vertex-sharing SiO_3N-tetrahedra forming 6er- and 4er-rings as fundamental building units (FBU). The nitrogen atoms are connected to three silicon atoms ($N^{[3]}$), while the oxygen atoms are either terminally bound ($O^{[1]}$) or bridge two silicon atoms ($O^{[2]}$) (numbers in superscripted square brackets after atoms indicate the coordination number of the atom in question). Two crystallographically independent Ba^{2+} sites are situated between the silicate layers. Luminescence investigations have shown that $Ba_3Si_6O_{12}N_2:Eu^{2+}$ exhibits excellent luminescence properties (emission maximum at ≈527 nm, full width at half maximum (FWHM) of ≈65 nm, low thermal quenching), which provides potential for industrial application in phosphor-converted light-emitting diodes (pc-LEDs). In-situ high-pressure and high-temperature investigations with synchrotron X-ray diffraction indicate decomposition of $Ba_3Si_6O_{12}N_2$ under these conditions. The band gap of $Ba_3Si_6O_{12}N_2:Eu^{2+}$ was measured to be 7.05 ± 0.25 eV by means of X-ray emission spectroscopy (XES) and X-ray absorption near edge spectroscopy (XANES). This agrees well with calculated band gap of 6.93 eV using the mBJ-GGA potential. Bonding to the Ba atoms is highly ionic with only the $4p_{3/2}$ orbitals participating in covalent bonds. The valence band consists primarily of N and O p states and the conduction band contains primarily Ba d and f states with a small contribution from the N and O p states.

Keywords: density functional calculations · high-pressure chemistry · luminescence · oxonitridosilicates · X-ray absorption spectroscopy

[a] C. Braun, M. Seibald, S. L. Börger, Dr. O. Oeckler, Prof. Dr. W. Schnick
Department Chemie
Lehrstuhl für Anorganische Festkörperchemie
Ludwig-Maximilians-Universität München
Butenandtstrasse 5–13 (D), 81377 München (Germany)
Fax: (+49) 89-2180-77440
E-mail: wolfgang.schnick@uni-muenchen.de

[b] T. D. Boyko, Prof. Dr. A. Moewes
Department of Physics and Engineering
University of Saskatchewan, 116 Science Place
Saskatoon, Saskatchewan, S7N 5E2 (Canada)

[c] Dr. G. Miehe
Technische Universität Darmstadt
Fachbereich Material- und Geowissenschaften
Fachgebiet Disperse Feststoffe
Petersenstr. 23, 64827 Darmstadt (Germany)

[d] Dr. A. Tücks
Philips Technologie GmbH, Forschungslaboratorien
Solid State Lighting, Weisshausstr. 2, 52066 Aachen (Germany)

Supporting information for this article is available on the WWW under http://dx.doi.org/10.1002/chem.201000660.

Introduction

Nitrido- and oxonitridosilicates as well as binary silicon nitride (e.g., Si_3N_4,[1–3] SiAlONs,[4] $Sr_2Si_5N_8$:Eu^{2+},[5–7] $Eu_2Si_5N_8$[8,9]) are known to exhibit interesting physical[10,11] and luminescence properties.[12–16] During the last ten years, Eu^{2+}-doped nitrido- and oxonitridosilicates emerged as promising materials applicable for phosphor-converted light-emitting diodes (pc-LEDs) owing to their high chemical and physical stability, their extraordinary quantum efficiency of the luminescence process (up to $\approx$95%), and their very low thermal quenching. Namely $M_2Si_5N_8$:Eu^{2+}[6,7,12,17–19] and $MSi_2O_2N_2$:Eu^{2+} (M = alkaline earth metal)[20–24] are excellent examples for highly effective red-orange (2-5-8) and yellow-green (1-2-2-2) phosphors, respectively.[25] Thereby, the first warm white all-nitride pc-LED has been realized, exhibiting unprecedented color quality and stability with temperature and drive.[12] Another important red phosphor is the nitridoaluminosilicate $CaAlSiN_3$:Eu^{2+}[26,27] and its derivatives. As the quest for higher energy efficiency represents one of the most fundamental and exigent challenges to be solved by modern science and technology, it becomes apparent that the search for novel and ecologically acceptable energy sources is indispensable. Addressing this challenge, LEDs become more and more important due to their ongoing improved efficiency, their remarkable durability as well as their environmentally friendly production process and waste disposal. Nowadays AlGaInP-based LEDs are accessible emitting in the red to yellow range of the spectrum. It was not before the pioneering work of Nakamura in the 1990s that the technological access to efficient blue LEDs was provided.[28,29] Further band-gap engineering has made AlGaInN-based LEDs accessible emitting in the UV to green range of the spectrum. The concept of down conversion of blue light from InGaN LEDs by suitable color converters (i.e., phosphors) is appropriate for efficient lighting[30] and provides monochrome light of high color purity, especially in the wavelength range in which direct emitting LEDs are relatively inefficient ("yellow gap"). The spectral position of the emission of these down-conversion phosphors doped with rare-earth ions (e.g. Ce^{3+} or Eu^{2+}) depends very much on the ligand field of the rare-earth ions in the host lattice, with stronger covalent interactions driving the emission into the red region of the spectrum (nephelauxetic effect).

The new green-emitting phosphor $Ba_3Si_6O_{12}N_2$:Eu^{2+} has been discovered recently,[31,32] and its luminescence properties emerged to be promising[31,32] due to a small Stokes shift and a narrow emission band. However, no detailed crystallographic description based on single-crystal structure determination has been reported for $Ba_3Si_6O_{12}N_2$:Eu^{2+} nor for the related solid solutions with Sr as yet.

As phosphor materials may show phase transitions at elevated temperatures and/or pressures, in-situ investigations of these solids can decisively contribute to a better understanding and optimization of their manufacturing process. In addition, from a more fundamental point of view, new modifications with different luminescence properties (e.g., due to higher symmetry or a lower number of cation sites) may be revealed by applying non-ambient reaction conditions. These aspects are addressed in this work by a systematic investigation of the high-pressure and high-temperature behavior of $Ba_3Si_6O_{12}N_2$:Eu^{2+}.

Furthermore, important material properties (e.g., conductivity, optical absorption, chemical bonding, energy gap) are determined by the electronic structure. For example, the band gap of efficient phosphors must be large enough to avoid the lowest Eu d states being too close to the conduction band, which can result in thermal ionization of the photoexcited 5d-electron of Eu^{2+}. Therefore, the local partial density of states (LPDOS) of $Ba_3Si_6O_{12}N_2$:Eu^{2+} has been probed by soft X-ray spectroscopy (SXS) utilizing synchrotron radiation, namely by X-ray absorption near edge spectroscopy (XANES) and X-ray emission spectroscopy (XES), and is compared to our theoretical calculations within the density functional theory (DFT) framework.

Results and Discussion

Synthesis: Two different methods for sample synthesis were applied:

1) Mixtures of MCO_3 (M = Ba,Sr), SiO_2 and an excess of α-Si_3N_4 were heated in a radio-frequency (RF) furnace[33] at maximum temperatures of 1425 °C under nitrogen atmosphere according to the reaction below [Eq. (1)].

$$3\,(Ba,Sr)CO_3 + 4.5\,SiO_2 + 1.5\,\alpha\text{-}Si_3N_4 \xrightarrow[EuF_3]{1425\,^\circ C,\ N_2} (Ba,Sr)_3Si_6O_{12}N_2 : Eu^{2+} + 3\,CO_2 + \alpha\text{-}Si_3N_4 \quad (1)$$

During synthesis EuF_3 was used as a dopant. The reaction product was inhomogeneous, but contained single-crystals of $(Ba,Sr)_3Si_6O_{12}N_2$:Eu^{2+}, suitable for X-ray structure analysis

2) A more homogeneous bulk product of highly crystalline material (in this case without europium) was obtained from $BaSi_2O_2N_2$[23] (synthesis with small impurities of different Ba oxosilicates and α-Si_3N_4 according to reference [23]) by high-pressure/high-temperature (HP/HT) synthesis employing the multianvil press technique[34–36] at a pressure of 14 GPa and 1200 °C according to the reaction below [Eq. (2)].

$$BaSi_2O_2N_2 : Eu^{2+} + 2\,BaO + 4\,SiO_2 + \alpha\text{-}Si_3N_4 \rightarrow Ba_3Si_6O_{12}N_2 : Eu^{2+} + \alpha\text{-}Si_3N_4 \quad (2)$$

The atomic ratio M:Si:O:N = 3:6:12:2 of $Ba_3Si_6O_{12}N_2$ was confirmed by EDX measurements (see Experimental Section). However, samples obtained by high-pressure synthesis did not contain single-crystals suitable for X-ray diffraction analysis.

Table 1. Crystallographic data for $Ba_3Si_6O_{12}N_2$, $Ba_{2.56}Sr_{0.44}Si_6O_{12}N_2$ and $Ba_2SrSi_6O_{12}N_2$.[a]

Formula	$Ba_3Si_6O_{12}N_2$	$Ba_{2.56}Sr_{0.44}Si_6O_{12}N_2$	$Ba_2SrSi_6O_{12}N_2$
M_r [g mol^{-1}]	800.58	778.70	750.86
crystal system	trigonal	trigonal	trigonal
space group	$P\bar{3}$ (no. 147)	$P\bar{3}$ (no. 147)	$P\bar{3}$ (no. 147)
a [Å]	7.5218(1)	7.4830(6)	7.4624(2)
c [Å]	6.4684(1)	6.4513(5)	6.4234(2)
V [Å^3]	316.935(8)	312.84(4)	309.78(9)
Z	1	1	1
ρ_{calcd} [g cm^{-3}]	4.195	4.133	4.025
μ [mm^{-1}]	9.857	10.474	11.230
$F(000)$	362	355	344
crystal size [mm^3]	0.07×0.05×0.03	0.01×0.01×0.02	0.04x 0.04×0.02
T [K]	293(2)	293(2)	293(2)
2θ range [°]	6.28–60.78	6.28–54.80	6.30–67.52
total reflns	3294	1423	4591
independent reflns	625	479	838
observed reflns	482	338	757
parameters	36	38	38
GOF	0.921	0.919	1.072
R values [$I>2\sigma(I)$]	$R1=0.0256$	$R1=0.0389$	$R1=0.0165$
	$wR2=0.0479$	$wR2=0.0609$	$wR2=0.0327$
R values (all data)	$R1=0.0406$	$R1=0.0764$	$R1=0.0210$
	$wR2=0.0506$	$wR2=0.0718$	$wR2=0.0340$
max/min residual electron density [e Å^{-3}]	1.660/−1.146	1.422/−1.138	0.678/−0.558

[a] Lattice parameters for $Ba_3Si_6O_{12}N_2$ were taken from the Rietveld refinement based on powder diffraction data. The refined compositions for the solid solution series are: $Ba_{2.56(2)}Sr_{0.44(2)}Si_6O_{12}N_2$ and $Ba_{2.01(2)}Sr_{0.99(2)}Si_6O_{12}N_2$.

Structure determination: The crystal structure of $Ba_3Si_6O_{12}N_2$:Eu^{2+} and its solid-solution series $Ba_{3-x}Sr_xSi_6O_{12}N_2$ (with $x\approx0.4$ and 1) was solved by direct methods[37] and refined[38] in space group $P\bar{3}$ (no. 147) by using anisotropic displacement parameters for all atoms. The atomic parameters for Ba and Sr occupying the same site in the solid solution were constrained to be equal. However, the site occupancies were refined and the presence of Eu^{2+} in the structure (2 mol%) was neglected in these refinements. The details of the single-crystal structure refinement are listed in Table 1. Occupied Wyckoff sites and refined atomic coordinates from the single-crystal diffraction data are shown in the Supporting Information (Table S1). The interatomic distances and angles are within the typical range, selected data are given in Table 2.

Table 2. Selected bond lengths [in Å] and angles [in °] of $Ba_3Si_6O_{12}N_2$, $Ba_{2.56}Sr_{0.44}Si_6O_{12}N_2$ and $Ba_2SrSi_6O_{12}N_2$ derived from single-crystal data (standard deviations in parentheses).

	$Ba_3Si_6O_{12}N_2$	$Ba_{2.56}Sr_{0.44}Si_6O_{12}N_2$	$Ba_2SrSi_6O_{12}N_2$
Ba1−O2 (6×)	2.744(3)	2.687(5)	2.660(2)
Ba2−O2 (3×)	2.819(3)	2.815(5)	2.819(2)
Ba2−O2 (3×)	2.902(3)	2.902(6)	2.884(2)
Ba2−N1 (2×)	2.997(6)/3.471(6)	3.02(2)/3.44 (2)	3.017(3)/3.407(3)
Si1−O2 (1×)	1.587(3)	1.582(6)	1.586(2)
Si1−O1 (2×)	1.649(3)/1.650(4)	1.635(5)/1.651(6)	1.644(2)/1.647(2)
Si1−N1 (1×)	1.735(2)	1.737(3)	1.7311(6)
O2-O1-O1	134.6(5)	133.9(3)	133.2(8)
O2-N1-O2	86.3(4)	87.0(2)	87.7(5)
O1-N1-O1	160.1(5)	158.8(2)	158.0(5)

The refined crystal structure of $Ba_3Si_6O_{12}N_2$ solved by single-crystal diffraction was confirmed by X-ray powder diffraction on a sample obtained from HP/HT synthesis. Crystallographic data and details of the Rietveld refinement[39] are listed in Table 3 and in the Experimental Section. The observed and calculated X-ray powder diffraction patterns as well as their difference curve after Rietveld refinement are shown in Figure 1.

Structure description: A detailed insight into the crystal structure of $Ba_3Si_6O_{12}N_2$ is required to understand its luminescent properties. Here a comprehensive crystallographic structure description is presented, which is based on the structure refinements described above. The structural parameters given by Mikami et al. are basically correct.[31,32]

The structure of $Ba_3Si_6O_{12}N_2$ consists of layers of vertex-sharing SiO_3N tetrahedra of Q^3-type, building 6er- and 4er-rings as fundamental building units (FBU),[40] which leads to a degree of condensation of $\kappa=n(Si):n(O,N)=0.43$ for the $[Si_6O_{12}N_2]^{6-}$ substructure.

According to Pauling's rule[41] and $\{uB,3,1_{\infty2}\}[(Si_6^{[4]}O_6^{[1]}O_6^{[2]}N_{4/2}^{[3]})^{6-}]$[42,43] the O atoms bridge two Si atoms ($O^{[2]}$) or are terminally bound ($O^{[1]}$), respectively, whereas the N atoms connect three silicon tetrahedral centers ($N^{[3]}$; see Figure 2) (numbers in superscripted square brackets beside atoms indicate the coordination number of the atom in question). According to lattice energy calculations (Madelung part of lattice energy, MAPLE)[44–46] there

Table 3. Crystallographic data of $Ba_3Si_6O_{12}N_2$ derived from Rietveld refinement.

formula	$Ba_3Si_6O_{12}N_2$
M_r [g mol^{-1}]	780.54
crystal system	trigonal
space group	$P\bar{3}$ (no.147)
a [Å]	7.5218(1)
c [Å]	6.4684(1)
V [Å^3]	316.935(8)
Z	1
T [K]	293
data range, step width	$5\le2\theta\le60°$, 0.01°
background treatment	18 fixed background points
profile function	pseudo-Voigt (no. 7)
R_{Bragg}	1.56
GoF	1.6
reduced χ^2	2.66

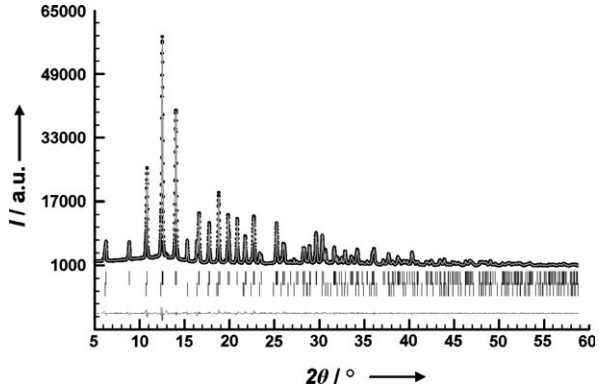

Figure 1. Observed (circles) and calculated (line) X-ray powder diffraction pattern together with their difference curve after Rietveld refinement ($\lambda = 0.709026$ Å). The upper row of reflection marks corresponds to $Ba_3Si_6O_{12}N_2$ and the lower one to β-Si_3N_4 (25% w/w).

is a clear assignment of N/O.[41,32] As expected the MAPLE of $Ba_3Si_6O_{12}N_2$ is almost identical with the sum of the respective MAPLE values of the constituting binary components BaO, SiO_2 and α-Si_3N_4 (see Table 4). The two crystal-

Table 4. Madelung part of lattice energy (MAPLE) values for $Ba_3Si_6O_{12}N_2$ (values given in kJ mol^{-1}).[a]

	$Ba_3Si_6O_{12}N_2$	BaO	SiO_2	α-Si_3N_4		
MAPLE	105684.75	3527.40	15347.60	53017.53		
atom[a]	$Ba1^{2+}$	$Ba2^{2+}$	Si^{4+}	$(O1^{[2]})^{2-}$	$(O2^{[1]})^{2-}$	$(N^{[3]})^{3-}$
MAPLE	1916.15	1890.63	9254.26	2987.00	2303.67	6358.86

total MAPLE ($Ba_3Si_6O_{12}N_2$) exptl	105684.75
total MAPLE ($3\,BaO + 4.5\,SiO_2 + 0.5\,\alpha$-$Si_3N_4$)	106155.17
difference Δ/%	0.44

[a] Typical partial MAPLE values [kJ mol^{-1}]: Ba^{2+}: 1500–2000, Sr^{2+}: 1500–2000, Si^{4+}: 9000–10200, $(O^{[2]})^{2-}$: 2400–2900, $(O^{[1]})^{2-}$: 2050–2800, $N^{[3]3-}$: 5200–6300.[72]

lographically independent Ba^{2+} ions occupy the Wyckoff sites 1*a* and 2*d*. They are situated between the silicate layers and are six- or sevenfold coordinated by (O,N) atoms, respectively (see Figure 3). The crystal structure of $Ba_3Si_6O_{12}N_2$, which is isotypic with recently discovered $Sr_3P_6O_6N_8$,[47] can be derived from the structure of β-Si_3N_4.[48] The isosteric Si_6N_{14} layers in β-Si_3N_4 are linked in the third dimension through SiN_4 tetrahedra. A formal derivation of the structure of $Ba_3Si_6O_{12}N_2$/$Sr_3P_6O_6N_8$ from β-Si_3N_4 can be achieved by a separation of the Si_6N_{14} layers in β-Si_3N_4 and intercalating Ba^{2+} ions (see Figure 2). Similar layered arrangements of Si/O/N tetrahedra with different degrees of condensation can be found in other Ba oxonitridosilicates as well, namely $Ba_3Si_6O_9N_4$[49] and $BaSi_2O_2N_2$.[23]

While in $BaSi_2O_2N_2$ only 3er-rings can be found, $Ba_3Si_6O_9N_4$[49] exhibits a structure related to $Ba_3Si_6O_{12}N_2$, which however contains different 6er-rings and additional 3er-rings.[50]

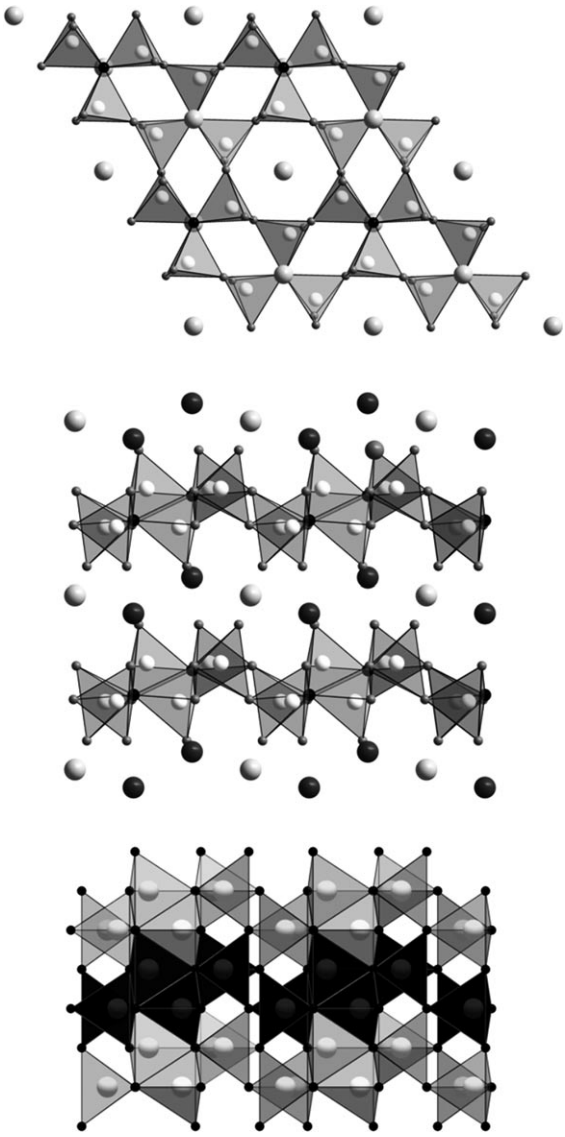

Figure 2. Comparison of $Ba_3Si_6O_{12}N_2$ and β-Si_3N_4: $Ba_3Si_6O_{12}N_2$ view along [001] (top), view along [010] (middle), and β-Si_3N_4 for comparison (bottom, view along [010]), removing every second Si-atom layer (black) and substituting the emerging terminal N-atoms by O-atoms results in layers, topologically similar to those in $Ba_3Si_6O_{12}N_2$ (Si atoms white, N black, Ba1 light gray, Ba2 dark gray and O gray).

The bond lengths Si–O/N in $Ba_3Si_6O_{12}N_2$ are in the typical range with 1.59–1.73 Å ($Ba_3Si_6O_9N_4$: Si–O/N = 1.60–1.75 Å,[49] $BaSi_2O_2N_2$: Si–O/N = 1.66–1.73 Å).[23] The distances Si–$O^{[1]}$ and Si–$O^{[2]}$ range between 1.59 Å for $O^{[1]}$ and 1.61–1.71 Å for $O^{[2]}$ and are therefore comparable with related Ba oxonitridosilicates (e.g. $Ba_3Si_6O_9N_4$: Si–$O^{[1]}$: 1.60 Å, Si–$O^{[2]}$: 1.65 Å,[49] $BaSi_2O_2N_2$: Si–$O^{[1]}$: 1.66 Å).[23] Within the tetrahedra, the Si–$N^{[3]}$ distance is, as expected, the longest one with 1.73 Å ($Ba_3Si_6O_9N_4$: Si–$N^{[3]}$ = 1.73–1.75 Å,[49] $BaSi_2O_2N_2$: Si–$N^{[3]}$ 1.72–1.73 Å).[23] The (O,N)-Si-(O,N) angles range from 103–116° and correspond well with other Ba oxonitridosilicates ($Ba_3Si_6O_9N_4$: 103–114°,[49] $BaSi_2O_2N_2$: 99–118°).[23] Compared to other Ba oxonitridosilicates the

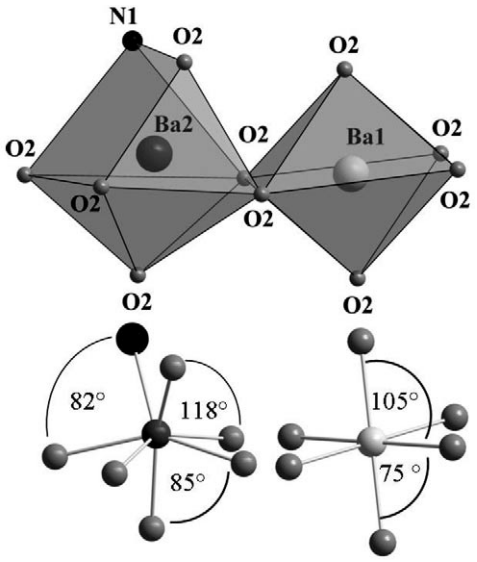

Figure 3. Coordination polyhedra and the corresponding angles of the two different Ba sites in $Ba_3Si_6O_{12}N_2$ (N atoms black, Ba1 light gray, Ba2 dark gray and O gray).

Si-N[3]-Si angle in $Ba_3Si_6O_{12}N_2$ (118°) is in the same range as in $Ba_3Si_6O_9N_4$ (118–120°)[49] and $BaSi_2O_2N_2$ (116–121°).[23] Cation coordination polyhedra in $Ba_3Si_6O_9N_4$ and $Ba_3Si_6O_{12}N_2$ are very similar as well.

In $Ba_3Si_6O_{12}N_2$ the oxygen atoms in the coordination sphere of Ba1 form a trigonal antiprism, which can be described as well as a distorted octahedron with six equal distances (Ba1[6]–O = 2.74 Å), but some angles (see Figure 3) deviating from 90° ($Ba_3Si_6O_9N_4$: Ba1[6]–O = 2.69–2.82 Å).[49] The coordination polyhedron around Ba2 can be described for $Ba_3Si_6O_{12}N_2$ as well as for $Ba_3Si_6O_9N_4$ as a capped distorted octahedron ($Ba_3Si_6O_{12}N_2$: Ba2[7]–O/N = 2.82–3.00 Å, $Ba_3Si_6O_9N_4$: Ba2[7]–O/N = 2.70–3.16 Å).[49]

In contrast to $Ba_3Si_6O_9N_4$, $Ba_3Si_6O_{12}N_2$ features excellent luminescence properties. Mikami[32] has suggested that this may be due to the longer Ba–N distances and a lower energy host absorption band of $Ba_3Si_6O_9N_4$ in comparison to $Ba_3Si_6O_{12}N_2$.

Solid-solution series of $Ba_{3-x}Sr_xSi_6O_{12}N_2:Eu^{2+}$: The influence of the Ba^{2+} substitution by Sr^{2+} in the solid-solution series $Ba_{3-x}Sr_xSi_6O_{12}N_2:Eu^{2+}$ (with $x \approx 0.4$ and 1) has been studied. In $Ba_{3-x}Sr_xSi_6O_{12}N_2:Eu^{2+}$ a substitution of Ba^{2+} by smaller Sr^{2+} mainly affects the Ba1 site (see Figure 3), which might be due to the smaller coordination number of this site. The substitution of Ba^{2+} by Sr^{2+} significantly influences the bond length Ba1/Sr1-O2, which decreases with increasing amount of Sr^{2+} ($Ba_3Si_6O_{12}N_2$: 2.74 Å, $Ba_2SrSi_6O_{12}N_2$: 2.66 Å) as the silicate layers approach along [001] upon substitution. Thereby, the curvature of the corrugated layers increases as well, especially around the Ba1/Sr1 sites. Table 2 shows the interatomic distances of selected atoms for $Ba_3Si_6O_{12}N_2$, $Ba_{2.56}Sr_{0.44}Si_6O_{12}N_2$ and $Ba_2SrSi_6O_{12}N_2$, respectively.

High-pressure and high-temperature behavior: In-situ high-pressure and high-temperature studies of luminescent materials were shown to be useful in optimizing the manufacturing process of several (oxo-)nitridosilicate phosphors. Therefore, ex-situ and in-situ investigations of $Ba_3Si_6O_{12}N_2$ were performed from 0.15 to 18 GPa and temperatures ranging from 100 to 1500 °C in order to evaluate the stability. This should be representative for the Ba/Sr solid-solution series as well. Ex-situ investigations at ambient conditions on HP/HT treated samples in the range from 9 to 18 GPa and at temperatures from 800 to 1200 °C using a Walker-type multi-anvil press were carried out. Formation of small amounts of β-Si_3N_4 besides $Ba_3Si_6O_{12}N_2$ indicate that $Ba_3Si_6O_{12}N_2$ might not be stable above 14 GPa. In-situ high-pressure X-ray diffraction investigations at the synchrotron (MAX80, Beamline F2.1 Desy/Hasylab Hamburg) confirmed the instability of $Ba_3Si_6O_{12}N_2$ and elucidated the underlying mechanism. Above 0.15 GPa decomposition into the related Ba oxonitridosilicate $BaSi_4O_6N_2$[51] was identified already at room temperature. This suggests that the formation of at least one amorphous phase is likely, since no other crystalline phase could be observed, particularly no Si_3N_4. The quantity of crystalline $BaSi_4O_6N_2$ increased in comparison to the remaining $Ba_3Si_6O_{12}N_2$ as the pressure was increased. At 9 GPa the sample showed distinct signs of amorphization, which was reversible after pressure release. Again at ambient pressure the powder pattern indicates mainly $Ba_3Si_6O_{12}N_2$; however, slight traces of $BaSi_4O_6N_2$ still could be detected. Therefore, the pressure-induced transformation from $Ba_3Si_6O_{12}N_2$ into $BaSi_4O_6N_2$ is mostly reversible. The same transformation is also observed at elevated temperatures (≈0.15 GPa) and the relative amount of $BaSi_4O_6N_2$ increases from 100 to 1500 °C successively. Furthermore, above 1200 °C two other decomposition products emerge: $BaSi_2O_2N_2$[23] and β-Si_3N_4.[48]

The temperature- and pressure-induced transformations of $Ba_3Si_6O_{12}N_2$, as observed under in-situ conditions, mainly agree with the final products detected ex-situ after HP/HT treatment. The formation of β-Si_3N_4 results from excursion to high temperatures above about 1200 °C (or at high pressures already at lower temperatures), either as a result of the instability of $Ba_3Si_6O_{12}N_2$ or from crystallization of initially amorphous and therefore in XRD not detectable Si_3N_4.

Luminescence: Samples of $Ba_3Si_6O_{12}N_2$ were doped with 2 mol% Eu^{2+} in order to study photoluminescence. $Ba_3Si_6O_{12}N_2:Eu^{2+}$ exhibits an intense green body color due to $4f^7(^8S_{7/2}) \rightarrow 4f^6 5d$ absorption of Eu^{2+} in the blue to green spectral range. Under near-UV to blue light irradiation a saturated green emission band with a peak wavelength of ≈527 nm is observed (full width at half maximum (FWHM) ≈65 nm). The broad excitation band enables efficient excitation at wavelengths below 450 nm.

The excitation (PLE) and emission (PE) spectra of several samples of $Ba_{3-x}Sr_xSi_6O_{12}N_2:Eu^{2+}$ are shown in Figures 4 and 5. For $x = 0$ the broad emission band almost matches the

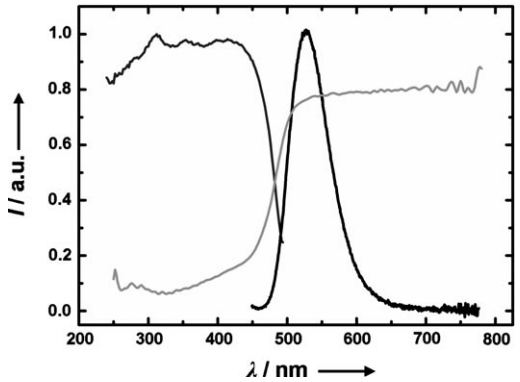

Figure 4. Excitation (gray), reflectance (light gray) and emission (black) spectra of $Ba_3Si_6O_{12}N_2$: Eu^{2+} (2 mol% Eu^{2+}).

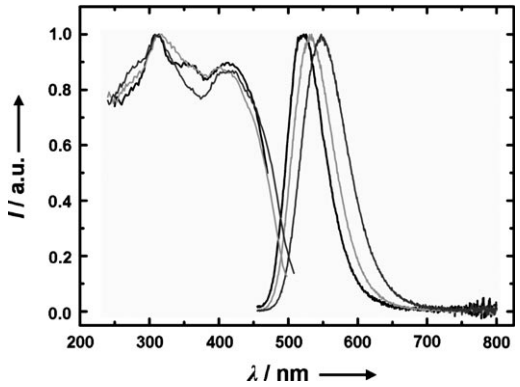

Figure 5. Excitation (PLE) and emission (PE) spectra of $Ba_{3-x}Sr_xSi_6O_{12}N_2$:$Eu^{2+}$ (several samples) with varying Sr contents. Excitation and emission spectra with 0% Sr are depicted in black, with 11% Sr in light gray, with 34% Sr in dark gray.

spectrum of Eu^{2+}-activated $BaSrSiO_4$:Eu^{2+} phosphors[52] and resembles typical Eu^{2+} spectra observed for other oxonitridosilicate compounds (e.g., $MSi_2O_2N_2$:Eu^{2+}).[53] For 11% Sr the emission spectrum nearly coincides with that of $SrSi_2O_2N_2$:Eu^{2+}. The spectral half-width of 2310 cm^{-1} (0% Sr) lies between the values observed for $BaSi_2O_2N_2$:Eu^{2+} (1340 cm^{-1}) and $SrSi_2O_2N_2$:Eu^{2+} (2423 cm^{-1}).[53] The former exhibits an exceptionally small FWHM value that corresponds to direct emitting cyan-green LEDs and can be attributed to the presence of only one very symmetrical crystallographic M^{2+} site as well as a small Stokes shift.

$Ba_3Si_6O_{12}N_2$:Eu^{2+} has a Stokes shift of $\approx$2600 cm^{-1} which is higher than the values for $BaSi_2O_2N_2$:Eu^{2+} (1030 cm^{-1}), but significantly lower than the Stokes shift of $SrSi_2O_2N_2$:Eu^{2+} (4740 cm^{-1}).[53] Partial substitution of Ba by Sr causes a noticeable red-shift and broadening of the emission band (see Table 5). As expected, the unit cell contracts with increasing amounts of Sr^{2+} (see crystallographic data, Table 1). Typically, such a unit-cell contraction involves decreasing interatomic distances between Eu^{2+} and its ligands and thus results in a larger crystal field strength at the activator site, leading to a red-shift of the emission band. Another factor that may affect the spectral shift and half-width

Table 5. Peak emission wavelength and spectral half-width of $Ba_{3-x}Sr_xSi_6O_{12}N_2$, depending on the partial substitution of Ba by Sr (Eu^{2+} content 2%).

Sr concentration [%]	λ_{max} [nm]	FWHM [cm^{-1}]
0	523	2310
11	532	2360
34	549	2510

is the presence of two different crystallographic sites, Ba1 and Ba2, which exhibit slightly different coordination (see Figure 3) and interatomic distances (see Table 2).

Due to their smaller but very similar ionic radii, Sr^{2+} as well as Eu^{2+} (compared to Ba^{2+}) should both preferentially occupy the distorted octahedral Ba1 site. Unless more than 1/3 of Ba is substituted by Sr and Eu, Eu^{2+} can always compete with the larger Ba^{2+} for the smaller Ba1 site. The spectral shift in the Ba/Sr-mixed compound is mainly caused by a unit-cell contraction. The increase in spectral width at higher Sr concentration can be attributed to an increasing Stokes shift. However, Mikami et al. suggested emission from Eu^{2+} primarily occupying the Ba2 site.[32]

Band structure and density of states: The band structure calculations (Figure 6) indicate that the material has an indirect band gap of 4.80 eV (using GGA), which is in good agree-

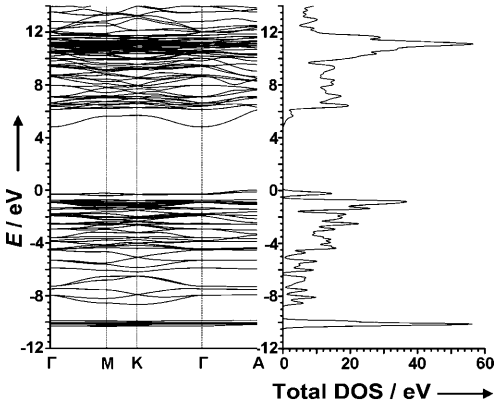

Figure 6. The total density of states (right, measured in states/eV-unit cell) and the band structure (left) of $Ba_3Si_6O_{12}N_2$:Eu^{2+} show the calculated direct (5.08 eV) and indirect (4.80 eV, A–Γ) band-gap values. The density of states (DOS) is broadened by a Gaussian function with a FWHM of 0.1 eV to aid in visual analysis.

ment with the previously reported value of 4.63 eV[32] using GGA. The band gap calculated using a modified Becke-Johnson potential with GGA (mBJ-GGA)[54] is 6.93 eV and accounts for the typical underestimation of the band gap. The modified potential is a semi-local exchange potential that allows for the correct calculation of the band gap in insulators and semiconductors. This potential is ab initio and requires no further input during the calculation. The total density of states (DOS) and partial DOS is derived from integrating momentum space and is shown for all atomic sites

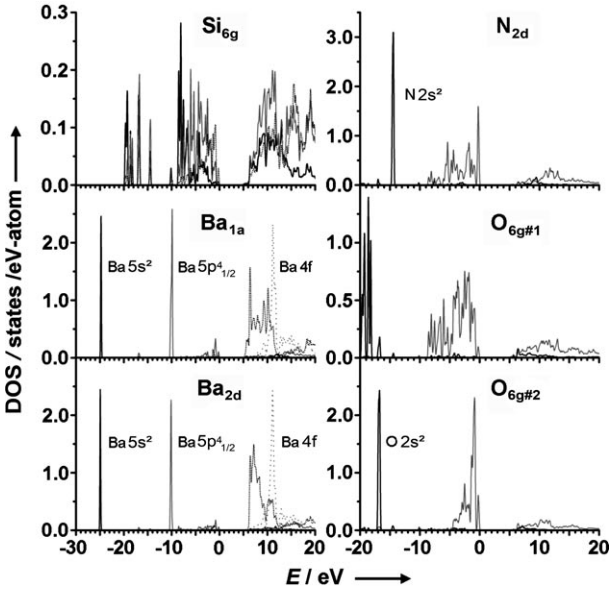

Figure 7. The density of states (DOS) is split into atomic site and electron symmetry contributions. The panels are labelled according to their Wyckoff site, furthermore the $O_{6g\#1}$ site refers to the site that forms bridging bonds to silicon. The s states are displayed black (solid), p states gray (solid), d states black (dotted) and f states gray (dotted). The DOS were broadened with a constant Gaussian of 0.1 eV FWHM and displayed in energy scale such that 0 eV corresponds to top of the valence band (i.e., the filled states). The large intensity peaks were scaled; the Ba_{1a} 5s states (reduced by 80%), $5p_{1/2}$ states (reduced by 80%), 4f states (reduced by 80%), and the Ba_{2d} 5s states (reduced by 85%), $5p_{1/2}$ states (reduced by 88%), 4f states (reduced by 80%).

in Figure 6 and 7, respectively. The DOS shows that $Ba_3Si_6O_{12}N_2$ exhibits a mixture of ionic bonding and weak covalent contributions. The Ba 5s electrons are highly localized and exhibit orbital-like behavior with no bonding. There is no indication of any Ba 6s states, thus the respective electrons of Ba are fully transferred to the N and O anion sites. The Ba 5p states are split by total angular momentum; the *j=1/2* are highly localized and non-bonding, while the *j=3/2* participate largely in the valence band (VB) covalent bonds with a small degree of participation in the conduction band (CB). The Ba 4f states play a key role in the formation of the CB, exhibiting a large peak (localized concentration of states) buried 5 eV into the CB. The CB states that are situated below 10 eV are primarily unfilled Ba 5d states. The Si s,p,d states show a large degree of hybridization with the O and N sites in conjunction with a large amount of charge transfer to the anion sites. The N and O sites suggest weak covalent bonds to the Si atoms; the N_{2d} and $O_{6g\#2}$ 2s states are highly localized with little or no bonding, but the N and O p states have a large degree of hybridization. The $O_{6g\#1}$ 2s states, however, show an affinity to form covalent bonds with Si, extending further to the $O_{6g\#1}$ 2p band as well. The N and O 2p states make up the majority of the VB with modest contribution to the CB.

Band-gap determination using soft X-ray spectra: The participation of the N and O p states in both the VB and CB makes studying the K-edge spectra of these elements an excellent probe for the electronic structure properties in general and the band gap in particular. We will first focus on the oxygen spectra.

Figure 8 shows the O K-edge soft X-ray spectroscopy measurements; this includes the O Kα X-ray emission spectra (XES) and O 1s X-ray absorption near edge spectra (XANES). There are three distinct features labelled d–g (see Figure 8) in the $Ba_3Si_6O_{12}N_2:Eu^{2+}$ O 1s XANES spectrum. The calculated O 1s XANES spectrum reproduces all the marked features and the general shape of the experimental spectrum very well. The true XANES spectrum consists of a summation of two spectra from the two non-equivalent O sites. These O 1s binding energies differ by 1.92 eV, owing to the different local symmetry (bridging bonds and tetrahedral bonds), which was determined with density functional theory (DFT) calculations. However, the energy separation seen in the measured XANES spectra is 1.76 eV, owing to the effect of an O 1s core hole. There is a small disagreement between the calculated and measured spectrum, mainly feature f (see Figure 8) is more intense in the measured spectrum than in the calculated spectrum. The added intensity is due to a third contributing spectrum, which is most likely from SiO_2 contamination. One of the

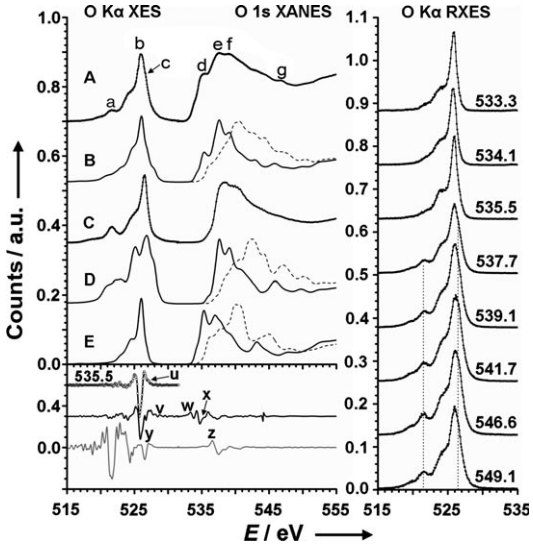

Figure 8. Non-resonant O Kα XES and O 1s XANES (left), and resonant O Kα XES (right) of A) measured $Ba_3Si_6O_{12}N_2:Eu^{2+}$, B) total calculated $Ba_3Si_6O_{12}N_2:Eu^{2+}$, C) measured SiO_2, D) calculated $O_{6g\#1}$ site, and E) calculated $O_{6g\#2}$ site are shown. The main features in the O Kα XES and O 1s XANES spectra for $Ba_3Si_6O_{12}N_2:Eu^{2+}$ are marked a–g. The right panel shows the resonant excitation energy of O Kα XES with the excitation energy indicated above each spectrum. The dashed lines indicate the contribution from SiO_2. The effect of the core hole is demonstrated with the simulated XANES spectra without the inclusion of the core hole, this is displayed as the dashed line plot in the left panel. The second derivatives of the experimental spectra are displayed in the lower left panel. The valence band (E_v) and conduction band (E_c) edges are indicated on the scatter line (the resonant XES spectra with the excitation energy indicated above, $u=O_{6g\#2}:E_v$), the solid black line (the experimental $Ba_3Si_6O_{12}N_2:Eu^{2+}$ spectra, $v=O_{6g\#1}:E_v$, $w=O_{6g\#1}:E_c$, $x=O_{6g\#1}:E_c$) and the gray line plots (the experiment SiO_2 spectra, $y=SiO_2:E_v$, $z=SiO_2:E_c$).

starting materials for synthesis of $Ba_3Si_6O_{12}N_2:Eu^{2+}$ is α-Si_3N_4, and there are significant amounts left after synthesis. Also, this material forms a surface SiO_2 layer under atmosphere readily, which will provide a spectral contribution to the O 1s XANES spectrum. This contamination and the two non-equivalent O sites were explored further with resonant XES. In the O Kα XES spectrum of $Ba_3Si_6O_{12}N_2:Eu^{2+}$ three spectral features can be found. Feature c (see Figure 8) is very subtle and is a high-energy shoulder that has been increased in intensity due to SiO_2 contamination. The low-energy peak a (see Figure 8) not seen in the simulated spectrum is also due to SiO_2. The two non-equivalent O sites are shifted by the difference in the 1s binding energy mentioned above (and not corrected for core hole effect since it is not present in the XES final state). In these spectra the excitation energy is tuned to resonant features of the XANES spectra. This allows the excitation of specific atomic sites within the lattice. Feature a in the O Kα resonant XES increases in intensity with excitation energies of 555.1 to 541.7 eV. The 541.7 eV excitation corresponds to the maximum absorption cross section in SiO_2, which is why the SiO_2 feature is the most intense. Feature c (see Figure 8) also increases in intensity, which is due to SiO_2 and confirms that SiO_2 is present on the surface. Tuning the excitation to even lower energy reduces the contributions of these peaks.

At an excitation energy of 535.5 eV, the emission spectrum changes drastically showing no signs of the $O_{6g\#1}$ site or the features of the SiO_2 contamination. The emission stems now purely from the $O_{6g\#2}$ p states and matches the calculated spectrum perfectly.

The lower energy resonant XES spectra are the same except that there are contributions from the other O atoms in the material; these are more apparent since the absorption cross sections of all the O atom sites are very low. These results suggest that the calculated spectrum for XES and XANES are correct if we properly consider the SiO_2 contamination.

The use of XES and XANES spectra to determine the top of the valence and bottom of the conduction band is not trivial due to the inherent experimental broadening mechanisms, difficulties in energy calibration, and the effect of the core hole on the absorption spectra. The energy positions of the conduction and valence band edges are determined by taking the second derivative of the experimental spectra (see Figure 8) and the first peak (above the level of noise) in the second derivative is used as the edge location.[55] The comparison of the SiO_2 second derivative to the non-resonant $Ba_3Si_6O_{12}N_2:Eu^{2+}$ shows that the SiO_2 valence band edge is located somewhere between the two edges of the oxygen non-equivalent sites. The conduction band edge of SiO_2 is much higher in energy than $Ba_3Si_6O_{12}N_2:Eu^{2+}$ (this is due to the very large band gap) and should present no problem for determining the bottom of the conduction band of $Ba_3Si_6O_{12}N_2:Eu^{2+}$ with O 1s XANES. The top of the valence band, however, can be more accurately determined by using resonant XES. Since the valence band edge of the $O_{6g\#1}$ site is very close to SiO_2, we determined the edge of the $O_{6g\#2}$ site. The O Kα XES spectrum with excitation energy of 535.5 eV is used to determine the $O_{6g\#2}$ site valence band edge; this was shown earlier to resemble the calculated spectrum best for that site. The edge locations of the $O_{6g\#1}$ are determined from the site splitting that is calculated, which makes the band gaps identical. The determined band gap for this site is 7.10 ± 0.20 eV and the corresponding VB and CB edge values are listed in Table 6. The details of the band-gap determination are further discussed in the experimental section.

Table 6. Band-gap determination using data from XES and XANES spectra in conjunction with DFT results. The sites are labelled according to their Wyckoff sites. The measured valence band and conduction edge locations are presented. The core hole effect has been rounded to the nearest 0.05 eV, and the final value of the band gap is average of the two independent determined values of the O K-edge and N K-edge. The measured band gap is compared the values obtained using GGA-PBE and mBJ-GGA.

	N_{2d}	$O_{6g\#1}$	$O_{6g\#2}$
valence band edge [eV]	394.45 ± 0.15	528.45 ± 0.15	526.55 ± 0.15
conduction band edge [eV]	401.20 ± 0.15	535.10 ± 0.15	533.35 ± 0.15
core hole shift [eV]	0.25	0.45	0.30
site band gap [eV]	7.00 ± 0.20	7.10 ± 0.20	7.10 ± 0.20
average measured band gap [eV]		7.05 ± 0.25	
calculated band gap (GGA-PBE) [eV]		4.80	
calculated band gap (mBJ-GGA) [eV]		6.93	

We now turn to the discussion of the nitrogen spectra. The N 1s XANES spectrum of $Ba_3Si_6O_{12}N_2:Eu^{2+}$ exhibits three features k–m (see Figure 9), which are reproduced well in the calculated $Ba_3Si_6O_{12}N_2:Eu^{2+}$ N 1s XANES spectrum. The position of feature l is slightly distorted, because of the presence of α-Si_3N_4 (as discussed previously). The addition of this spectrum increases the spacing between the features k and l in the experiment with comparison to the calculated N 1s XANES spectrum. Feature m remains relatively unchanged because the α-Si_3N_4 N 1s XANES spectrum is very smooth in this region. The effect of this impurity is readily seen in the N Kα XES spectra. The non-resonant N Kα XES spectrum displays the features h–j, which are reproduced in the calculated spectrum as well (see Figure 9). There remains still moderate agreement between features i and j in experiment; however feature h is overestimated in the calculated spectrum. This can be explained with the consideration of α-Si_3N_4 contribution to the measured spectrum. Feature h is present in the calculated spectrum and appears not to be present in the measured spectrum. However, this feature is present and has been removed due to the summation of $Ba_3Si_6O_{12}N_2:Eu^{2+}$ and β-Si_3N_4. Furthermore, it is enhanced with selective excitation as seen in the resonant XES spectra. Many of the resonant N Kα XES spectra look very similar except for the two excited at 404.4 and 407.3 eV. In these spectra features h and i are enhanced and provide better agreement with the calculated spectrum. These spectra are the result of exciting on the two resonant features k and l in the N 1s XANES spec-

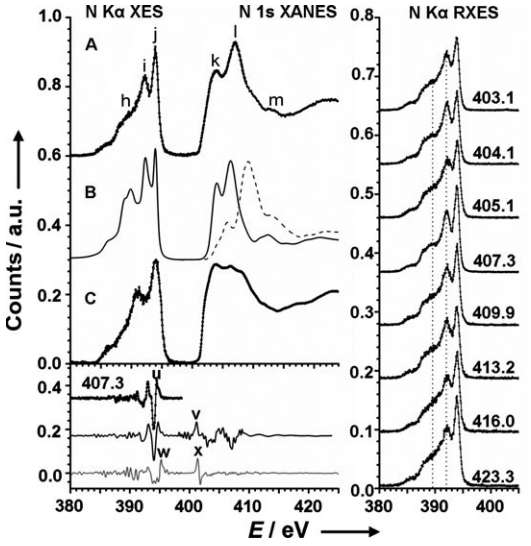

Figure 9. Non-resonant N Kα XES and N 1s XANES (left), and resonant N Kα XES (right) of A) measured $Ba_3Si_6O_{12}N_2:Eu^{2+}$, B) total calculated $Ba_3Si_6O_{12}N_2:Eu^{2+}$, and C) measured α-$Si_3N_4$ are shown. The main features in the N Kα XES and N 1s XANES spectra for $Ba_3Si_6O_{12}N_2:Eu^{2+}$ are denoted h–m. The panel on the right hand side shows the resonant N Kα XES with the excitation energy indicated above each spectrum. The dashed lines indicate the peaks that result from the remaining α-Si_3N_4. The effect of the core hole is demonstrated with the simulated XANES spectra without the inclusion of the core hole, this is displayed as the dashed line plot. The second derivatives of the experimental spectra are displayed in the lower left panel. The valence band (E_v) and conduction band (E_c) edges are indicated on the scattered line (the resonant XES spectra with the excitation energy indicated above, u = N_{2d}:E_v), the solid black line (the experimental $Ba_3Si_6O_{12}N_2:Eu^{2+}$ spectra, v = N_{2d}:E_c) and the grey line plots (the experiment α-Si_3N_4 spectra, w = Si_3N_4:E_v, x = Si_3N_4:E_c).

trum, which are attributed to $Ba_3Si_6O_{12}N_2:Eu^{2+}$. This shows that the calculated spectrum is a very reasonable representation of the material with the consideration of α-Si_3N_4 that is present in the sample. The band gap has also been determined using the N sites. The DOS results show that 1) both the N and O electron states contribute to the band gap and 2) that the band gaps determined from the N and O site should be identical. The same method used for the oxygen sites and explained above is applied to the nitrogen sites; resonant XES again is used to preferentially excite the nitrogen atoms that are part of the $Ba_3Si_6O_{12}N_2:Eu^{2+}$ matrix. The second derivative of α-Si_3N_4 has a valence band edge that is higher in energy than $Ba_3Si_6O_{12}N_2:Eu^{2+}$ and the conduction band edge is higher in energy as well. The band gaps of these materials are predicted to be very similar[32,56] and the offset in the spectra is due to the differences in the nitrogen-bonding environment (the N 1s binding energy is slightly different). The α-Si_3N_4 contribution to the N Kα XES spectrum is removed as much as possible through resonant XES to obtain the best determination of the N valence band edge.

The excitation energy of 407.3 eV of the resonant XES spectrum was used to determine the valence band edge. The band gap obtained is identical to the one obtained for the O K-edge 7.00 ± 0.2 eV and the corresponding VB and CB edge values are summarized in Table 6. To summarize, the average band gap obtained from both oxygen and nitrogen sites is 7.05 ± 0.25 eVThese agree with each other within the experimental precision (± 0.25 eV), and are determined from the experimental spectra with a small correction derived in our calculations to account for the presence of the core hole and non-equivalent sites.

Conclusion

The high color purity, the small thermal quenching[57] at elevated temperatures, and the intense green color with a broadband emission spectrum peaking at ≈527 nm and a FWHM of ≈65 nm renders $Ba_3Si_6O_{12}N_2:Eu^{2+}$ a promising phosphor for pc-LED based general illumination and display applications.[12,31,32,52,58,59]

Especially important for the luminescence properties is the band gap being large enough to avoid the lowest Eu d states being too close to the conduction band and the thermal ionization of the photoexcited 5d electrons of Eu^{2+}.[32] In the case of $Ba_3Si_6O_9N_4:Eu^{2+}$ this effect becomes very apparent; the narrower band gap and a smaller crystal field splitting provide quite different optical properties compared to $Ba_3Si_6O_{12}N_2:Eu^{2+}$. Although the crystal structure and chemical formula of $Ba_3Si_6O_9N_4$[49] appear rather similar to the one of $Ba_3Si_6O_{12}N_2$, its luminescence properties render it inapplicable for use in pc-LEDs.

Structural studies at high-pressure and high-temperature reveal a decomposition of $Ba_3Si_6O_{12}N_2$, mainly into $BaSi_4O_6N_2$, and can explain the sintering behavior of this material.

The band gap is an important parameter for the luminescent properties. Synchrotron-based soft X-ray emission and absorption spectra were measured and compared to the respective density functional theory calculations. The calculated band gap from these calculations is 4.80 eV (indirect) using GGA-PBE; however, this method strongly underestimates the band gap. The XES and XANES spectra were calculated and show excellent agreement with the experimental ones when the presence of the core hole is taken into account. The calculations were also used to discuss and determine energy shifts due to the presence of the core hole and site splitting in the two non-equivalent oxygen sites. These considerations allow a reliable experimental determination of the band gap of $Ba_3Si_6O_{12}N_2:Eu^{2+}$, which is found to be 7.05 ± 0.25 eV for both the N and O K-edge measurements. This value agrees with the calculated band gap of 6.93 eV (mBJ-GGA) within experimental error. Furthermore, the valence band is shown to be primarily made up of N and O p states and the conduction band of primarily Ba d and f states, with a small contribution from the N and O p states. The bonding of the Ba atoms is highly ionic with only the $4p_{3/2}$ participating in covalent bonds, which makes this material ideal for cation substitution.

As a consequence of this, our future research will focus on in-situ investigations of material properties to intentionally access new compounds with respect to the specific requirements for efficient phosphors.

Experimental Section

High-pressure synthesis of $Ba_3Si_6O_{12}N_2$ and ex-situ high-pressure investigations: The high-pressure synthesis of $Ba_3Si_6O_{12}N_2$ was carried out by using the multianvil technique[34–36] with a hydraulic press (Voggenreiter, Mainleus). Cr_2O_3-doped MgO-octahedra (Ceramic Substrates & Components, Isle of Wight) with an edge length of 10 mm were used. Eight truncated tungsten carbide cubes separated by pyrophyllite gaskets served as anvils for the compression of the octahedra. The truncation edge length was 5 mm. Powder of ambient-pressure $BaSi_2O_2N_2$[23] was loaded into a cylindrical capsule of hexagonal boron nitride (Henze, Kempten) with a capacity of 4 mm^3 and sealed with a BN cap. The capsule was centered within two nested graphite tubes, which acted as an electrical resistance furnace. The remaining volume at both ends of the sample capsule was filled out with two cylindrical pieces of magnesium oxide. The arrangement was placed into a zirconia tube and then transferred into a pierced MgO octahedron. Two plates of molybdenum provided electrical contact for the graphite tubes. The assembly was compressed up to 14 GPa at room temperature within 2.5 h and then heated up to 1000 °C within 12 min. Under these conditions, the sample was held for 12 min and cooled down to 600 °C within 30 min. The sample was then quenched to room temperature, followed by decompression over 9.6 h. By this procedure about 5 mg of $Ba_3Si_6O_{12}N_2$ were obtained as a dark gray substance. The temperature was calculated from the electrical power applied to the furnace which was determined on the basis of calibration curves from measurements with $W_{97}Re_3W_{75}Re_{25}$ thermocouples, as described in ref.[60] Ex-situ high-pressure measurements were performed at 9, 12, 14, 16, and 18 GPa, respectively.

Single-crystal synthesis: To synthesize single crystals of $Ba_3Si_6O_{12}N_2$, $BaCO_3$ (0.49 mmol, powder, Alfa Aesar, 98 %), SiO_2 (0.75 mmol, Aerosil® A380 nano-powder, Degussa, ≥ 99.8 %), crystalline α-Si_3N_4 (0.25 mmol, excess, powder, UBE Industries, 98 %), and EuF_3 (0.01 mmol, powder, Aldrich Chemical, 99.99 %) were mixed together, ground in an agate mortar, and placed into a tungsten crucible inside a glovebox under Ar atmosphere (Unilab, Fa. Braun, Garching, O_2 < 1 ppm, H_2O < 1 ppm). The crucible was then heated inductively in the water cooled quartz reactor of a radio-frequency furnace (typ TIG 10/100, frequency: 100 kHz, max. electrical output: 10 kV, Huettinger, Freiburg) under N_2 atmosphere (purified by passing columns of silica gel (Merck), KOH (Merck, ≥85 %), molecular sieve (Merck, 4 Å) and P_4O_{10} (Roth, Granulopent®) to 1150 °C with a rate of about 23 °C min^{-1}. The temperature was then increased to 1350 °C over a period of 9 h, kept at this temperature for 1 h, and was then again increased to 1400 °C over a period of 20 h. After another temperature enhancement to 1425 °C over a period of 1 h, the sample was cooled down to 650 °C with a rate of about 0.33 °C min^{-1} to offer best conditions for good crystallinity. $Ba_3Si_6O_{12}N_2$ showing green luminescence when excited with UV-light was obtained in the shape of a hard and flat ingot coated with a transparent Matrix of glassy like α-Si_3N_4 which has to be removed to achieve single crystals. To get samples of the solid-solution series $SrCO_3$ (powder, Alfa Aeser, 98 %) was used beside the other reactants.

Single-crystal X-ray diffraction: Mechanically isolated green luminescent ($Ba_3Si_6O_{12}N_2$:Eu^{2+}) and yellow greenish (($Ba,Sr)_3Si_6O_{12}N_2$:Eu^{2+}) single-crystals obtainend by RF-furnace synthesis were mounted on glass fibres and checked for quality by Laue photographs on a Buerger precession camera. Intensity data were collected on a STOE IPDS-I diffractometer with imaging plate detector and graphite monochromator ($Ba_3Si_6O_{12}N_2$) or on a Nonius Kappa-CCD diffractometer with graded multilayer X-ray optics ($Ba_{2.56}Sr_{0.44}Si_6O_{12}N_2$ and $Ba_2SrSi_6O_{12}N_2$), both using $Mo_{K\alpha}$ radiation ($\lambda = 0.71073$ Å). Semiempirical absorption corrections based on equivalent reflections were applied[61] before the structures were solved by direct methods in space group $P\bar{3}$ (no. 147).[37] Full-matrix least-squares refinements of models developed from the initial solutions were executed with SHELXL[38] with anisotropic displacement parameters for all atoms. Further details of the crystal structure investigations may be obtained from Fachinformationszentrum Karlsruhe, 76344 Eggenstein-Leopoldshafen, Germany (fax: (+49)7247-808-666; e-mail, crysdata@fiz-karlsruhe.de, http://www.fiz-karlsruhe.de/request_for_deposited_data.html) on quoting the depository numbers CSD-421322 ($Ba_3Si_6O_{12}N_2$), CSD-421323 ($Ba_2SrSi_6O_{12}N_2$), and CSD-421324 ($Ba_{2.56}Sr_{0.44}Si_6O_{12}N_2$).

Powder X-ray diffraction: X-ray diffraction experiments on powder samples of $Ba_3Si_6O_{12}N_2$ were performed on a STOE STADI P powder diffractometer in Debye–Scherrer geometry with Ge(111)-monochromatized $Mo_{K\alpha1}$ radiation ($\lambda = 0.709026$ Å). The sample was enclosed in a glass capillary with 0.1 mm diameter. A Rietveld refinement was carried out using the program package Fullprof.[39] Estimated standard deviations were calculated in agreement with reference [62]. The atomic parameters agreed with the single crystal data within the standard deviations (2σ). β-Si_3N_4[48] was included as a second phase (24.5 % w/w) (see Figure 1).

In-situ high-pressure and high-temperature measurements: In-situ high-pressure measurements were performed with the multianvil high-pressure apparatus MAX80 (NRD Tsukuba, Japan), which is located at the Hamburger Synchrotronstrahlungslabor (HASYLAB, Beamline F.2.1) for in-situ high-pressure and high-temperature X-ray diffraction investigations. Energy-dispersive diffraction patterns were recorded by using white X-rays from the storage ring DORIS III. The pressure was measured by using the high-pressure equation of state for admixed NaCl by Decker.[63] The beamline was equipped with a Ge solid-state detector, situated at the press frame and tracking the adjustment of the whole apparatus in relation to the X-ray beam.

The multianvil apparatus was equipped with six tungsten carbide anvils that were driven by a 2.500 N uniaxial hydraulic ram. The top and bottom anvil were driven directly, the lateral anvils by two load frames and four reaction bolsters. The maximum pressure for the 8 mm cube setup was approximately 9 GPa with temperatures up to 1600 °C, which were produced by an internal graphite heater. The high-pressure cell consisted of a cube made of boron epoxy resin and the gaskets between the anvils are formed from the boron epoxy cube's material during the runs. The high-pressure cell was filled with the ground sample, the graphite heater, the pressure standard (NaCl) and the thermocouple, which was insulated by boron nitride. The sample was surrounded by rings made from pyrophyllite for electrical insulation and as a quasi-hydrostatic pressure transmitting medium. Copper rings contacted the heater at the top and bottom anvils.

Luminescence: Photoluminescence measurements were carried out with a spectrofluorimeter, equipped with a 150 W Xe lamp, two 500 mm Czerny–Turner monochromators, 1800 1 mm lattices and 250/500 nm lamps, providing a spectral range from 230–820 nm.

EDX measurements: The carbon coated sample was examined with a scanning electron microscope (SEM) JSM-6500F (Joel, Japan, maximum acceleration voltage 30 kV). Qualitative and semi-quantitative elemental analyses were carried out using an energy dispersive spectrometer (Model 7418, Oxford Instruments, United Kingdom).

Soft X-ray spectroscopy: The XANES measurements were performed at the SGM[64] beamline of the Canadian Light Source, Saskatoon, Saskatchewan (Canada). The XANES measurements were taken in total fluorescence yield mode with an experimental resolving power $E/\Delta E$ of approximately 5000. The XES measurements were performed with the soft X-ray fluorescence spectrometer at Beamline 8.0.1[65] of the Advanced Light Source, Berkeley, California (USA). The resolving power in the emission experiments was approximately 700. All measurements were taken with the sample orientated 30° from normal with respect to the incoming beam. A powder sample was pressed into freshly scraped indium foil in order to minimize background contributions from oxygen during the measurements. The measured spectra were calibrated with reference spectra from well-characterized samples. The N K-edge spectra were calibrated using hexagonal BN, using the peaks near the band gap with assigned values 392.6 eV for XES and 394.4 eV for XANES, respectively. The O K-edge spectra were calibrated with BGO ($Bi_4Ge_3O_{12}$) with peak

values near to the band gap assigned as 526.4 eV and 532.7 eV for XES and XANES spectra, respectively. The ab initio density functional theory (DFT) calculations employed the commercially available WIEN2k DFT software.[66] This code uses Kohn–Sham methodology with spherical wave functions to model core orbitals, linearized augmented plane waves (LAPW), semi-core, and valence states.[67,68] The exchange interactions used were the generalized gradient approximation (GGA) of Perdew–Burke–Ernzerhof[69] and the modified Becke–Johnson potential within GGA (mBJ-GGA).[54] We note that this approximation is known to strongly underestimate the band gap, but can provide good agreement with the shape of the valence and conduction bands and therefore the measured soft X-ray spectra. The proper simulation of the XES and XANES measurements requires that one considers the final state of the system during the measurement. The final state of the XES measurement can be approximated as the ground state of the system; all of the core electrons are present. The simulation of this measurement requires no modification of the system. The final state after a XANES measurement included a missing core electron. The effects from this core hole were modelled in the current work by including a single core hole inside of a supercell. This supercell was a larger cell made by replicating the unit cell along its common axes approximating the core hole density that is seen in experimental measurements.

The only input to the calculation was the crystal structure as determined by X-ray diffraction. The ground-state calculations were carried out on the unit cell with a 1000 k-point mesh. The sphere sizes used to define the core electrons were 2.400, 1.800, 1.4810, and 1.1590 Bohr for Ba, Si, N, and O, respectively, and the energy cut off was set to −6.0 Ryd. The size of the supercell used was $2\times1\times1$ of the unit cell (46 atoms) with a 100 k-point mesh. Normally a larger supercell would be used, but due the large interstitial space between the Ba ations and the N or O anions extensive memory resources ($\approx$ 6 GB memory per k-point) was required for the plane wave expansion, and so the size of the supercell had to be limited in order to achieve convergence in a reasonable time frame without limiting the plane wave basis size.

The simulated spectra were broadened to facilitate comparison with the experiments. A combination of Lorentzian and Gaussian functions was used to emulate the core-hole lifetime broadening[70] ($\Delta E=0.10$ eV for oxygen and $\Delta E=0.09$ eV for nitrogen), final-state lifetime broadening[71] (this is variable broadening and scales with the energy squared from the central point being the conduction band edge) with a scaling factor of 0.30 for N and 0.20 for O, instrumental broadening with a scaling factor of 0.30 for N and 0.20 for O, and instrumental broadening (this is resolution of the beamline and spectrometer) with a FWHM of 0.40 at 400 eV and 0.40 at 520 eV for the spectrometer, respectively, and 0.80 at 400 eV and 0.80 at 520 eV for the monochromator, respectively.

The band-gap determination used a combination of experimentally measured and calculated results. There were three key considerations this study used when determining the band gap. 1) The VB and CB edge locations were determined by using the second derivative, which has been previously successful.[55] 2) The site splitting, which occurs because of non-equivalent core electron binding energy in non-equivalent sites was determined from DFT results. 3) The XANES measurements were strongly affected by the core hole present in the final state; again DFT calculations provide an estimate in the shift of the CB that is caused by the core hole. These three effects were added numerically to the initially determined band gap and provide a reliable estimate of the actual band gap.

Acknowledgements

The authors gratefully acknowledge financial support from the Fonds der Chemischen Industrie and the Deutsche Forschungsgemeinschaft (priority program SPP 1236, project SCHN 377/13), Germany. We further would like to thank Anke Großer (LMU München) for experimental help, Christian Lathe (Geoforschungszentrum Potsdam) for his help at the Beamline F2.1 of the Hamburger Synchrotronstrahlungslabor at the Deutsches Elektronen Synchrotron (DESY) and for the provided beamtime, Christian Minke (LMU München) for the EDX measurements and Thomas Miller and Dr. Peter Mayer (LMU München) for X-ray single-crystal data collection. Furthermore, we gratefully acknowledge the Natural Sciences and Engineering Research Council of Canada (NSERC) and the Canada Research Chair program for their support in this research. We also thank the Advanced Light Source and Canadian Light Source along with their staff and support for helping us conduct this research.

[1] H. Lange, G. Wötting, G. Winter, *Angew. Chem.* **1991**, *103*, 1606–1625; *Angew. Chem. Int. Ed. Engl.* **1991**, *30*, 1579–1597.
[2] A. Zerr, G. Miehe, G. Serghiou, M. Schwarz, E. Kroke, R. Riedel, H. Fueß, P. Kroll, R. Boehler, *Nature* **1999**, *400*, 340–342.
[3] M. Schwarz, G. Miehe, A. Zerr, E. Kroke, B. T. Poe, H. Fuess, R. Riedel, *Adv. Mater.* **2000**, *12*, 883–887.
[4] W. Schnick, *Int. J. Inorg. Mater.* **2001**, *3*, 1267–1272.
[5] R.-J. Xie, N. Hirosaki, T. Suehiro, F.-F. Xu, M. Mitomo, *Chem. Mater.* **2006**, *18*, 5578—5583.
[6] M. Zeuner, P. J. Schmidt, W. Schnick, *Chem. Mater.* **2009**, *21*, 2467–2473.
[7] M. Zeuner, F. Hintze, W. Schnick, *Chem. Mater.* **2009**, *21*, 336–342.
[8] H. Huppertz, W. Schnick, *Acta Crystallogr. Sect. C* **1997**, *53*, 1751–1753.
[9] H. A. Höppe, H. Trill, B. D. Mosel, H. Eckert, G. Kotzyba, R. Pöttgen, W. Schnick, *J. Phys. Chem. Solids* **2002**, *63*, 853–859.
[10] S. Hampshire in *Materials Science and Technology, Vol. 11* (Eds.: R. W. Cahn, P. Haasen, E. J. Kramer), Wiley-VCH, Weinheim, **1994**.
[11] L.-O. Nordberg, M. Nygren, P.-O. Käll, Z. Shen, *J. Am. Ceram. Soc.* **1998**, *81*, 1461–1470.
[12] R. Mueller-Mach, G. Mueller, M. R. Krames, H. A. Höppe, F. Stadler, W. Schnick, T. Juestel, P. Schmidt, *Phys. Status Solidi A* **2005**, *202*, 1727–1732.
[13] T. Jüstel, H. Nikol, C. Ronda, *Angew. Chem.* **1999**, *111*, 3250–3271; *Angew. Chem. Int. Ed.* **1998**, *37*, 3084–3103.
[14] C. Ronda, *Luminescence: From Theory to Applications*, Wiley-VCH, Weinheim, **2008**.
[15] W. Schnick, *Phys. Status Solidi RRL* **2009**, *3*, A113–A114.
[16] R. Mueller-Mach, G. O. Mueller, M. R. Krames, O. B. Shchekin, P. J. Schmidt, H. Bechtel, C.-H. Chen, and O. Steigelmann, *Phys. Status Solidi RRL* **2009**, *3*, 215–217.
[17] T. Schlieper, W. Schnick, *Z. Anorg. Allg. Chem.* **1995**, *621*, 1037–1041.
[18] T. Schlieper, W. Milius, W. Schnick, *Z. Anorg. Allg. Chem.* **1995**, *621*, 1380–1384.
[19] H. A. Höppe, H. Lutz, P. Morys, W. Schnick, A. Seilmeier, *J. Phys. Chem. Solids* **2000**, *61*, 2001–2006.
[20] H. A. Höppe, F. Stadler, O. Oeckler, W. Schnick, *Angew. Chem.* **2004**, *116*, 5656–5659; *Angew. Chem. Int. Ed.* **2004**, *43*, 5540–5542.
[21] O. Oeckler, F. Stadler, T. Rosenthal, W. Schnick, *Solid State Sci.* **2007**, *9*, 205–212.
[22] F. Stadler, O. Oeckler, H. A. Höppe, M. H. Möller, R. Pöttgen, B. D. Mosel, P. Schmidt, V. Duppel, A. Simon, W. Schnick, *Chem. Eur. J.* **2006**, *12*, 6984–6990.
[23] J. A. Kechele, O. Oeckler, F. Stadler, W. Schnick, *Solid State Sci.* **2009**, *11*, 537–543.
[24] V. Bachmann, C. Ronda, O. Oeckler, W. Schnick, A. Meijerink, *Chem. Mater.* **2009**, *21*, 316–325.
[25] a) C.-C. Yang, C.-M. Lin, Y.-J. Chen, Y.-T. Wu, S.-R. Chuang, R.-S. Liu, S.-F. Hu, *Appl. Phys. Lett.* **2007**, *90*, 123503–1–3; b) R.-S. Liu, Y.-H. Liu, N. C. Bagkar, S.-F. Hu, *Appl. Phys. Lett.* **2007**, *91*, 061119/1–3; c) Y. Q. Li, A. C. A. Delsing, G. de With, H. T. Hintzen, *Chem. Mater.* **2005**, *17*, 3242–3248; d) Y. Q. Li, G. de With, H. T. Hintzen, *J. Mater. Chem.* **2005**, *15*, 4492–4496; e) B.-G. Yun, Y. Miyamoto, H. Yamamoto, *J. Electrochem. Soc.* **2007**, *154*, J320–J325; f) D. Becker, T. Fiedler, W. Hempel, F. Jermann (Patra Patent Treuhand), PCT Int. Appl., WO2007096333A1, **2007**; g) B.-G. Yun, K. Machida, H. Yamamoto, *J. Ceram. Soc. Jpn.* **2007**, *115*, 619–622; h) V. Bach-

mann, T. Juestel, A. Meijerink, C. Ronda, P. J. Schmidt, *J. Lumin.* **2006**, *121*, 441–449; i) A. C. A. Delsing, H. T. Hintzen, Y.-Q. Li (Osram Opto Semiconductors GmbH), PCT Int. Appl., WO2004030109A1, **2004**; j) T. Fiedler, F. Jermann (Patra Patent Treuhand), Ger. Offen., DE 102004051395A1, **2006**; k) H. Brunner, T. Fiedler, F. Jermann, J. Strauss, M. Zachau (Patra Patent Treuhand, Osram Opto Semiconductors GmbH), PCT Int. Appl., WO2005031797A2, **2005**; l) T. Fiedler, F. Jermann (Patra Patent Treuhand), PCT. Int. Appl., WO2005030905A1, **2005**; m) H. Brunner, T. Fiedler, F. Jermann, M. Zachau, B. Braune (Osram Opto Semiconductors GmbH, Patra Patent Treuhand), PCT Int. Appl., WO2005030904A1, **2005**; n) H. Brunner, T. Fiedler, F. Jermann, M. Zachau (Patra Patent Treuhand, Osram Opto Semiconductors GmbH), PCT Int. Appl., WO 2005030903A1, **2005**.

[26] X.-H. He, N. Lian, J.-H. Sun, M.-Y. Guan, *J. Mater. Sci.* **2009**, *44*, 4763–4775.

[27] M. Mikami, H. Watanabe, K. Uheda, S. Shimooka, Y. Shimomura, T. Kurushima, N. Kijima, *IOP Conf. Ser.: Mater. Sci. Eng.* **2009**, *1*, 012002–012012.

[28] S. Nakamura, T. Mukai, M. Senoh, *Appl. Phys. Lett.* **1994**, *64*, 1687–1689.

[29] T. Mukai, S. Nagahama, N. Iwasa, M. Senoh, T. Yamada, *J. Phys. Condens. Matter* **2001**, *13*, 7089–7098.

[30] H. A. Höppe, *Angew. Chem.* **2009**, *121*, 3626–3636; *Angew. Chem. Int. Ed.* **2009**, *48*, 3572–3582.

[31] S. Shimooka, K. Uheda, M. Mikami, N. Kijima, H. Imura, K. Horibe, PCT Int. Appl., WO088966A1, **2007**.

[32] M. Mikami, S. Shimooka, K. Uheda, H. Imura, N. Kijima, *Key Eng. Mater.* **2009**, *403*, 11–14.

[33] W. Schnick, H. Huppertz, R. Lauterbach, *J. Mater. Chem.* **1999**, *9*, 289–296.

[34] H. Huppertz, *Z. Kristallogr.* **2004**, *219*, 330–338.

[35] D. Walker, M. A. Carpenter, C. M. Hitch, *Am. Mineral.* **1990**, *75*, 1020–1028.

[36] D. Walker, *Am. Mineral.* **1991**, *76*, 1092–1100.

[37] M. C. Burla, M. Camalli, B. Carrozzini, G. L. Cascarano, C. Giacovazzo, G. Polidori, R. Spagna, *J. Appl. Crystallogr.* **2003**, *36*, 1103–1103.

[38] G. M. Sheldrick, *Acta Crystallogr. Sect. A* **2008**, *64*, 112–122.

[39] Fullprof. 2k-version 4.40, J. Rodriguez-Carvajal, **2008**.

[40] L. B. McCusker, F. Liebau, G. Engelhardt, *Pure Appl. Chem.* **2001**, *73*, 381–394.

[41] P. E. D. Morgan, *J. Mater. Sci.* **1986**, *21*, 4305–4309.

[42] F. Liebau, *Structural Chemistry of Silicates*, Springer, Berlin, **1985**.

[43] H.-J. Klein, F. Liebau, *J. Solid State Chem.* **2008**, *181*, 2412–2417.

[44] R. Hoppe, *Angew. Chem.* **1970**, *82*, 7–16; *Angew. Chem. Int. Ed. Engl.* **1970**, *9*, 25–34.

[45] a) R. Hoppe, *Angew. Chem.* **1966**, *78*, 52–63; *Angew. Chem. Int. Ed. Engl.* **1966**, *5*, 95–106; b) R. Hoppe, *Z. Naturforsch. A* **1995**, *50*, 555–567; c) C. Weiß, R. Hoppe, *Z. Anorg. Allg. Chem.* **1996**, *622*, 1019–1026.

[46] MAPLE, Madlung Part of Lattice Energy (Program), Version 4, R. Hübenthal, University of Gießen (Germany), **1993**.

[47] S. J. Sedlmaier, J. Schmedt auf der Günne, W. Schnick, *Dalton Trans.* **2009**, 4081–4084.

[48] R. Grün, *Acta Crystallogr. Sect. B* **1979**, *35*, 800–804.

[49] F. Stadler, W. Schnick, *Z. Anorg. Allg. Chem.* **2006**, *632*, 949–954.

[50] The term dreier (3er) ring was coined by Liebau and is derived from the German word "drei", which means three; however, a dreier ring is not a three-membered ring, but a six-membered ring comprising three tetrahedral centers (Si) and three electronegative atoms (N). Similar terms exist for rings comprising four, five, and six tetrahedral centers (and the corresponding number of electronegative atoms), namely vierer (4er), fünfer (5er), and sechser (6er) rings, respectively. (F. Liebau, *Structural Chemistry of Silicates*, Springer, Berlin, **1985**.).

[51] C. Braun, H. Ehrenberg, T. D. Boyko, A. Moewes, W.Schnick, unpublished results.

[52] T. L. Barry, *J. Electrochem. Soc.* **1968**, *115*, 1181–1184.

[53] P. Schmidt, A. Tuecks, J. Meyer, H. Bechtel, D. Wiechert, R. Mueller-Mach, G. Mueller, W. Schnick, Philips Research Europe Aachen (Germany); Proceedings of SPIE—The International Society for Optical Engineering **2007**, 6669 (Seventh International Conference on Solid State Lighting **2007**), 66690P/1–9.

[54] F. Tran, P. Blaha, *Phys. Rev. Lett.* **2009**, *102*, 226401.

[55] E. Z. Kurmaev, R.G Wilks, A. Moewes, L.D Finkelstein, S. Shamin, J. N. Kunes, *Phys. Rev. B* **2008**, *77*, 165127–165131.

[56] Y. N. Xu, W. Y. Ching, *Phys. Rev. B* **1995**, *51*, 17379–17389.

[57] N. Kijima, Y. Shimomura, T. Kurushima, H. Watanabe, S. Shimooka, M. Mikami, K. Uheda, *J. Light Visual Environ.* **2008**, *32*, 202–205.

[58] K. Uheda, N. Hirosaki, H. Yamamoto, *Phys. Status Solidi A* **2006**, *203*, 2712–2717.

[59] R.-J. Xie, N. Hirosaki, T. Suehiro, F.-F. Xu, M. Mitomo, *Chem. Mater.* **2006**, *18*, 5578–5583.

[60] D. C. Rubie, *Phase Transitions* **1999**, *68*, 431–451.

[61] XPREP, Version 6.12, Siemens Analytical X-ray Instruments Inc., Madison, **1996**.

[62] J. F. Berar, P. Lelann, *J. Appl. Crystallogr.* **1991**, *24*, 1–5.

[63] D. L. Decker, *J. Appl. Phys.* **1971**, *42*, 3239–3244.

[64] J. J. Jia, T. A. Callcott, J. Yurkas, A. W. Ellis, F. J. Himpsel, M. G. Samant, J. Stöhr, D. L. Ederer, J. A. Carlisle, E. A. Hudson, L. J. Terminello, D. K. Shuh, R. C. C. Perera, *Rev. Sci. Instrum.* **1995**, *66*, 1394–1397.

[65] T. Regier, J. Krochak, T. K. Sham, Y. F. Hu, J. Thompson, R. I. R. Blyth, *Nucl. Instr. Methods Phys. Res. A* **2007**, *582*, 93–95.

[66] WIEN2k An Augmented Plane Wave+Local Orbitals Program for Calculating Crystal Properties, P. Blaha, K. Schwarz, G. K. H. Madsen, D. Kvasnicka, J. Luitz, Vienna University of Technology (Austria), Revised Edition, **2008**.

[67] K. Schwarz, P. Blaha, G. Madsen, *Comput. Phys. Commun.* **2002**, *147*, 71–76.

[68] K. Schwarz, P. Blaha, *Comput. Mater. Sci.* **2003**, *28*, 259–273.

[69] J. Perdew, K. Burke, M. Ernzerhof, *Phys. Rev. Lett.* **1996**, *77*, 3865–3868.

[70] M. O. Krause, J. H. Oliver, *J. Phys. Chem. Ref. Data* **1979**, *8*, 329–338.

[71] D. A. Goodings, R. Harris, *J. Phys. Pt. Sol. Stat. Phys. C* **1969**, *2*, 1808–1816.

[72] H. A. Höppe, Dissertation, Universität München (Germany), **2003**.

Received: March 15, 2010
Published online: July 28, 2010

